Non-peer-reviewed preprint submitted to EarthArXiv

EarthArXiv Preprint

Author ORCID: https://orcid.org/0009-0009-6367-4655
Corresponding author: O. L. Konovalov <konovalovol@bsu.by>
License: CC BY 4.0
Date: November 11, 2026

Activity-based excavation modelling in total Lagrangian SPH with pressure-dependent plasticity

O. L. Konovalov*
Applied Mathematics and Informatics, Belarusian State University, Minsk, Belarus

Abstract

We present an activity-based excavation model for underground mining simulations implemented within the total Lagrangian Smoothed Particle Hydrodynamics (TLSPH) framework of SoliDualSPHysics. The model introduces three key features: (1) a smooth cosine-based activity transition that gradually reduces the stiffness, mass, and gravitational loading of excavated particles; (2) a Drucker–Prager plasticity model with closed-form return mapping for pressure-dependent geomaterial behaviour; and (3) a stress diffusion stabilisation term that damps dynamic oscillations in the explicit time integration. The model is validated against the FEM code TOCHNOG using J_2 and Drucker–Prager plasticity. For J_2, the maximum equivalent plastic strain agrees within 10%. For Drucker–Prager, qualitative agreement is observed with quantitative overprediction attributed to the lower yield threshold at low confining pressure and the inherent dynamic overshoot of explicit time integration.

Keywords: SPH; Total Lagrangian; Excavation; Drucker–Prager; Plasticity; Stress diffusion; Geomechanics.

1 Introduction

Modelling underground excavation processes is a challenging problem in computational geomechanics. The removal of material from a rock or soil mass creates a void that triggers stress redistribution, plastic deformation, and potential collapse of the surrounding ground. Traditional finite element methods (FEM) handle this problem through element deactivation or remeshing, but both approaches introduce numerical artefacts: element deactivation creates artificial stress discontinuities at the excavation boundary, while remeshing propagates state variables with inevitable interpolation errors.

Mesh-free particle methods offer a natural alternative, as they do not require a mesh and can accommodate large deformations without remeshing. Among these, the Material Point Method (MPM) has been widely applied to excavation and slope stability problems, but it suffers from grid-crossing instabilities and requires a background grid. The Discrete Element Method (DEM) captures particulate behaviour but is computationally prohibitive for continuum-scale problems [1].

Smoothed Particle Hydrodynamics (SPH) is a fully mesh-free Lagrangian method originally developed for astrophysical flows [2] and later extended to solid mechanics. In

*Corresponding author: konovalovol@bsu.by; ORCID: https://orcid.org/0009-0009-6367-4655

the total Lagrangian SPH (TLSPH) formulation, all quantities are referred to the initial (undeformed) configuration, and the kernel interpolation operates on fixed neighbour lists. This avoids the particle deficiency and tensile instability problems that afflict the updated Lagrangian (ULSPH) formulation, particularly near free surfaces created by excavation [3, 4].

Several authors have applied SPH to geomechanical problems. Bui and Fukagawa [5] proposed an SPH method with Drucker–Prager plasticity for soil excavation using an updated Lagrangian formulation. Bui and Nguyen [6] provided a comprehensive review of SPH applications in geomechanics, from solid fracture to granular behaviour. However, these works employ ULSPH formulations with small-strain Jaumann stress rates, which fail to reproduce beam-like bending of the excavation roof: the kernel degrades near the free surface as neighbours in the current configuration are lost, and the Jaumann rate introduces errors under large rotations.

The recently developed SoliDualSPHysics code [7] extends DualSPHysics [8] with a TLSPH formulation for solid mechanics, including hyperelasticity, J_2 plasticity, and phase-field fracture. Its total Lagrangian kernel, evaluated in the reference configuration, maintains complete neighbour lists regardless of deformation, and its finite-strain formulation correctly captures large rotations — making it suitable for modelling roof bending and collapse in excavation problems.

In this work, we extend SoliDualSPHysics with three capabilities for underground excavation modelling:

1. An *activity-based excavation* mechanism that gradually reduces the stiffness, mass, and gravitational loading of excavated particles through a smooth cosine transition, avoiding the stress jumps associated with abrupt particle removal.

2. A *Drucker–Prager plasticity* model with a closed-form (non-iterative) return mapping, capturing the pressure-dependent shear strength of geomaterials.

3. A *stress diffusion* stabilisation term that damps dynamic oscillations in the explicit time integration, driving the solution toward the quasi-static regime.

The proposed model is validated against the open-source FEM code TOCHNOG [9], which provides both J_2 (von Mises) and Drucker–Prager plasticity in a quasi-static implicit framework. Two validation cases are presented: (1) a homogeneous soil block with an extraction chamber, using J_2 plasticity to isolate the excavation mechanism from the constitutive model; and (2) the same geometry with Drucker–Prager plasticity, demonstrating pressure-dependent failure.

The paper is organised as follows. Section 2 describes the TLSPH framework, the J_2 and Drucker–Prager constitutive models, the activity-based excavation mechanism, and the stress diffusion stabilisation. Section 3 presents the validation against TOCHNOG. Section 4 discusses the dynamic versus quasi-static behaviour, the role of the diffusion coefficient, and limitations. Section 5 concludes the paper.

2 Method

2.1 Total Lagrangian SPH framework

The excavation model is implemented within the total Lagrangian SPH (TLSPH) framework of SoliDualSPHysics, which extends DualSPHysics v5.2 to solid mechanics. In the

TLSPH formulation, all quantities are referred to the initial (undeformed) configuration $\mathbf{X}$. The deformation gradient is computed as

$$F_i^{kq} = \delta^{kq} + \frac{1}{\rho_{0i}} \sum_{j=1}^{N_i} m_{0j}\, u_{ji}^k \, \frac{\partial W_{0ij}}{\partial X_j^q}, \tag{1}$$

where $\mathbf{u} = \mathbf{x} - \mathbf{X}$ is the displacement, W_{0ij} is the corrected Wendland kernel evaluated in the reference configuration, and the summation extends over all neighbours j of particle i.

The momentum equation is discretised in the standard TLSPH symmetrised form:

$$\frac{dv_i^k}{dt} = \sum_{j=1}^{N_i} m_{0j} \left(\frac{P_i^{kq}}{\rho_{0i}^2} + \frac{P_j^{kq}}{\rho_{0j}^2} + \Pi_{ij}\delta^{kq} \right) \frac{\partial W_{0ij}}{\partial X_j^q} + g^k, \tag{2}$$

where $\mathbf{P} = \mathbf{FS}$ is the first Piola–Kirchhoff stress, $\mathbf{S}$ is the second Piola–Kirchhoff stress, and Π_{ij} is an artificial viscosity term.

2.2 Activity-based excavation

The excavation is modelled through an *activity factor* $\alpha \in [0, 1]$ that controls the residual stiffness of excavated particles. For each particle i, the excavation mask $\mathcal{M}_i \in \{0, 1\}$ identifies whether the particle lies within the excavation zone. For masked particles ($\mathcal{M}_i = 1$), the deformation gradient, stress, mass, and gravitational acceleration are scaled:

$$\mathbf{F}_i \leftarrow \alpha\, \mathbf{F}_i + (1 - \alpha)\, \mathbf{I}, \qquad \mathbf{S}_i \leftarrow \alpha\, \mathbf{S}_i, \tag{3}$$

where α is the activity factor. When $\alpha = 1$, the particle behaves as fully intact material; when $\alpha \to 0$, the particle approaches a stress-free, mass-free "ghost" state.

In the momentum equation (2), the contribution of an excavated neighbour j is scaled by a neighbour factor:

$$\tilde{\Pi}_{ij} = \mathcal{M}_j\, \alpha + (1 - \mathcal{M}_j), \tag{4}$$

so that excavated neighbours exert a reduced force $\alpha\, \mathbf{P}_j / \rho_{0j}^2$ on intact particles. For the excavated particle itself, the total acceleration is scaled:

$$\mathbf{a}_i \leftarrow \alpha \left(\mathbf{a}_i^{\text{int}} + \mathbf{g} \right), \tag{5}$$

where $\mathbf{a}_i^{\text{int}}$ is the internal (SPH + viscous) acceleration. This ensures that excavated particles gradually "freeze" as $\alpha \to 0$, preventing the spurious "spring" effect that arises when stress-free particles with full mass remain in the computational domain.

2.3 Gradual excavation transition

To avoid numerical instabilities caused by an abrupt stiffness reduction, the activity factor is transitioned smoothly from $\alpha = 1$ (intact) to $\alpha_{\text{final}} = 0.1$ (residual) over a prescribed duration T_{excav} using a cosine profile:

$$\alpha(t) = \begin{cases} 1, & t < t_{\text{start}}, \\ \alpha_{\text{final}} + (1 - \alpha_{\text{final}}) \dfrac{1 + \cos\left(\pi \dfrac{t - t_{\text{start}}}{T_{\text{excav}}} \right)}{2}, & t_{\text{start}} \le t < t_{\text{start}} + T_{\text{excav}}, \\ \alpha_{\text{final}}, & t \ge t_{\text{start}} + T_{\text{excav}}. \end{cases} \tag{6}$$

This ensures C^0 continuity at $t = t_{\text{start}}$ and $t = t_{\text{start}} + T_{\text{excav}}$, eliminating the stress jump that would otherwise trigger a blow-up of the explicit time integration.

2.4 J_2 plasticity with isotropic hardening

The baseline plasticity model available in SoliDualSPHysics is a finite-strain J_2 (von Mises) plasticity with linear isotropic hardening, based on the multiplicative decomposition of the deformation gradient [10]:

$$\mathbf{F} = \mathbf{F}_e \, \mathbf{F}_p, \tag{7}$$

where $\mathbf{F}_e$ and $\mathbf{F}_p$ are the elastic and plastic parts, respectively. The plastic deformation gradient $\mathbf{F}_p$ is stored as the primary internal variable and initialised to the identity tensor.

The elastic right Cauchy–Green tensor is computed from the multiplicative split:

$$\mathbf{C}_e = \mathbf{F}_p^{-T} \, \mathbf{C} \, \mathbf{F}_p^{-1}, \tag{8}$$

where $\mathbf{C} = \mathbf{F}^T \mathbf{F}$ is the total right Cauchy–Green tensor. Plastic incompressibility ($\det \mathbf{F}_p = 1$) is enforced, so $J_e = J$.

The deviatoric Mandel stress is

$$\mathbf{M}_{\text{dev}} = \mu \, \text{dev}(\bar{\mathbf{C}}_e), \qquad \bar{\mathbf{C}}_e = J_e^{-2/3} \, \mathbf{C}_e, \tag{9}$$

and the equivalent (von Mises) stress is

$$\sigma_{\text{eq}} = \sqrt{\tfrac{3}{2} \, \mathbf{M}_{\text{dev}} : \mathbf{M}_{\text{dev}}}. \tag{10}$$

The yield function with linear isotropic hardening reads

$$f = \sigma_{\text{eq}} - \sigma_y(\bar{\varepsilon}^p), \qquad \sigma_y(\bar{\varepsilon}^p) = \sigma_{y0} + H \, \bar{\varepsilon}^p, \tag{11}$$

where σ_{y0} is the initial yield stress, H is the hardening modulus, and $\bar{\varepsilon}^p$ is the accumulated equivalent plastic strain.

The return mapping employs an exponential-map predictor–corrector scheme operating directly on $\mathbf{F}_p$. The plastic multiplier $\Delta\gamma$ is determined by solving the nonlinear scalar consistency equation via an Illinois-modified regula–falsi bracketing iteration [11]. The plastic deformation gradient is updated via the exponential map

$$\mathbf{F}_p^{n+1} = \exp\!\big(\Delta\gamma \, \mathbf{N}^{\text{tr}}\big) \, \mathbf{F}_p^{n}, \tag{12}$$

followed by a volume-preserving projection $\mathbf{F}_p \leftarrow (\det \mathbf{F}_p)^{-1/3} \mathbf{F}_p$.

This J_2 model is pressure-independent: the yield threshold σ_y does not depend on the confining pressure I_1. While suitable for metals, this is inadequate for geomaterials, where shear strength increases with confining pressure. This motivates the Drucker–Prager extension.

2.5 Drucker–Prager plasticity

The constitutive response of the soil is described by the Drucker–Prager yield criterion, which captures the pressure-dependent shear strength characteristic of geomaterials. The yield function is

$$f = \alpha_\phi \, I_1 + \sqrt{J_2} - k_c, \tag{13}$$

where $I_1 = \mathrm{tr}(\mathbf{M})$ is the first invariant of the Mandel stress tensor, $J_2 = \frac{1}{2}\mathbf{M}_{\mathrm{dev}} : \mathbf{M}_{\mathrm{dev}}$ is the second deviatoric invariant, and α_ϕ, k_c are Drucker–Prager constants related to the cohesion c and friction angle ϕ through

$$\alpha_\phi = \frac{\tan\phi}{\sqrt{9 + 12\tan^2\phi}}, \qquad k_c = \frac{3c}{\sqrt{9 + 12\tan^2\phi}}. \tag{14}$$

For the plane-strain (2D) embedding used in this work, these constants correspond to the Drucker–Prager surface circumscribing the Mohr–Coulomb yield surface in plane strain.

Under gravitational loading with the tension-positive convention, $I_1 < 0$ (compressive), so the yield threshold at low confining pressure (near the excavation roof) reduces to $\sqrt{J_2} > k_c$, while at high confining pressure (deep in the soil) the term $\alpha_\phi I_1$ becomes strongly negative, raising the effective threshold and stabilising the material.

2.6 Closed-form return mapping

The plastic corrector employs a closed-form (non-iterative) return mapping. The plastic multiplier is

$$\Delta\lambda = \frac{f_{\mathrm{trial}}}{9\kappa\alpha_\phi\alpha_\psi + \mu}, \tag{15}$$

where α_ψ is the dilatancy factor (related to the dilation angle ψ analogously to α_ϕ) and μ is the shear modulus. For the present work, $\psi = 0$ (non-associated flow with zero dilatancy), simplifying the denominator to μ.

The plastic deformation gradient is updated via the exponential map:

$$\mathbf{F}_p^{n+1} = \exp(\Delta\lambda\,\mathbf{N}_{\mathrm{flow}})\,\mathbf{F}_p^n, \qquad \mathbf{N}_{\mathrm{flow}} = \frac{3}{2\sigma_{\mathrm{eq}}}\mathbf{M}_{\mathrm{dev}} + \alpha_\psi\mathbf{I}, \tag{16}$$

followed by a volume-preserving projection $\mathbf{F}_p \leftarrow (\det\mathbf{F}_p)^{-1/3}\mathbf{F}_p$. The equivalent plastic strain is accumulated as $\bar{\varepsilon}^{p,n+1} = \bar{\varepsilon}^{p,n} + \Delta\lambda$.

2.7 Stress diffusion stabilisation

Explicit time integration of the momentum equation under gravitational loading generates dynamic oscillations that can produce spurious stress peaks. These peaks are particularly problematic when combined with pressure-dependent yield criteria such as Drucker–Prager, where the yield threshold at low confining pressure is small and easily exceeded by transient stress fluctuations.

To mitigate this, a stress diffusion term is applied to the first Piola–Kirchhoff stress $\mathbf{P}_1$ between the constitutive update and the force computation:

$$\mathbf{P}_{1,i} \leftarrow \mathbf{P}_{1,i} + 2\zeta\,h\,c_s\,\Delta t\sum_{j=1}^{N_i}(\mathbf{P}_{1,i} - \mathbf{P}_{1,j})\frac{\mathbf{r}_{0,ij}\cdot\nabla_0 W_{ij}}{r_{0,ij}^2 + \eta^2} \tag{17}$$

where ζ is a dimensionless diffusion coefficient, h is the smoothing length, c_s is the speed of sound, $\mathbf{r}_{0,ij} = \mathbf{X}_i - \mathbf{X}_j$ is the reference-configuration distance, and $\eta = 0.1\,h$ is a regularisation parameter. The kernel gradient $\nabla_0 W_{ij}$ is pre-computed and stored in the neighbour pair arrays, and includes the particle volume $V_{0,j}$ as in the deformation gradient computation (1).

This term acts as a numerical viscosity that smooths high-frequency stress oscillations without permanently altering the stress state: at each time step, the stress is recomputed from the deformation gradient via the constitutive model, and the diffusion provides only a transient correction to the force computation.

2.8 Gravity ramp

To reduce dynamic oscillations during the initial loading phase, gravity is applied gradually through a linear ramp:

$$\mathbf{g}(t) = \min\left(\frac{t}{T_g}, 1\right)\mathbf{g}_\infty, \tag{18}$$

where T_g is the ramp duration and $\mathbf{g}_\infty = (0, 0, -9.81)\,\mathrm{m/s^2}$. In this work, $T_g = 30\,\mathrm{s}$. The ramp allows the soil mass to consolidate quasi-statically before the excavation begins, ensuring that the initial stress state is close to the lithostatic equilibrium.

2.9 Implementation

The excavation model is implemented in the SoliDualSPHysics codebase across eight source files. The Drucker–Prager constitutive model is added as `constitmodel = 4` alongside the existing St. Venant–Kirchhoff (1), Neo–Hookean (2), and J_2 plasticity (3) models. The model parameters — cohesion c, friction angle ϕ, and dilation angle ψ — are read from the XML configuration file.

The simulation uses a Wendland C2 kernel with $h/\Delta x = 1.414$, artificial viscosity coefficients $\beta_1 = 0.5$, $\beta_2 = 0$, and a CFL number of 0.1. The domain is $40 \times 40\,\mathrm{m}$ discretised with $\Delta x = 0.25\,\mathrm{m}$, yielding 25,921 particles. The excavation zone ($x \in [17, 23]$, $z \in [20, 24]$) is marked before the main loop. The activity factor transitions from 1.0 to 0.1 over $T_{\mathrm{excav}} = 5\,\mathrm{s}$, beginning at $t_{\mathrm{start}} = 35\,\mathrm{s}$ (after the gravity ramp completes). Gravity is $g = 9.81\,\mathrm{m/s^2}$ with a 30 s linear ramp. The bottom and lateral boundaries are fixed through velocity boundary conditions. The stress diffusion coefficient is $\zeta = 0.1$.

3 Validation

The proposed excavation model is validated against the open-source FEM code TOCHNOG [9], which solves the quasi-static equilibrium equations using an implicit Newton–Raphson scheme. Two validation cases are presented: (1) J_2 (von Mises) plasticity, to isolate the excavation mechanism from pressure-dependent effects; and (2) Drucker–Prager plasticity, representing a more realistic geomaterial behaviour.

3.1 Problem setup

The validation problem consists of a $40 \times 40\,\mathrm{m}$ soil block discretised with $\Delta x = 0.25\,\mathrm{m}$, yielding 25,921 particles in the SPH model. The material parameters are summarised in Table 1.

Table 1: Material parameters.

Parameter	Symbol	Value
Young's modulus	E	10 MPa
Poisson's ratio	ν	0.3
Density	ρ	2000 kg/m^3
Bulk modulus	κ	8.33 MPa
Shear modulus	μ	3.85 MPa
J_2 plasticity		
Yield stress	σ_{y0}	400 kPa
Hardening modulus	H	1 MPa
Drucker–Prager plasticity		
Cohesion	c	60 kPa
Friction angle	ϕ	20°
Dilation angle	ψ	0°

The excavation zone is a rectangular chamber of 6×4 m ($x \in [17, 23]$, $z \in [20, 24]$), centred horizontally in the domain. The excavation begins at $t_{\text{start}} = 35$ s and transitions over $T_{\text{excav}} = 5$ s. The bottom and lateral boundaries are fixed through velocity boundary conditions. Gravity is $g = -9.81\,\text{m/s}^2$ with a 30 s linear ramp. The stress diffusion coefficient is $\zeta = 0.1$.

3.2 J_2 plasticity: excavation mechanism validation

The J_2 validation isolates the excavation mechanism from pressure-dependent effects. With a yield stress of $\sigma_{y0} = 400$ kPa, the material behaves as an elastic–plastic solid with linear hardening, and the yield threshold is independent of confining pressure.

Table 2: Validation results: J_2 plasticity.

	SoliDualSPH	TOCHNOG	Error
Max subsidence u_z [m]	1.6	1.3	+23%
Max $\bar{\varepsilon}^p$	0.091	0.10	−9%
Kinetic energy [J]	1.3	—	—

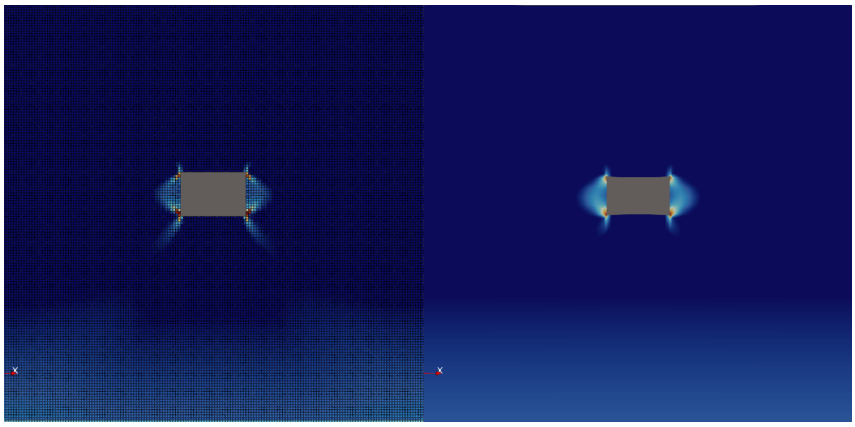


Figure 1: Equivalent plastic strain $\bar{\varepsilon}^p$ field: (a) SoliDualSPH, (b) TOCHNOG. J_2 plasticity.

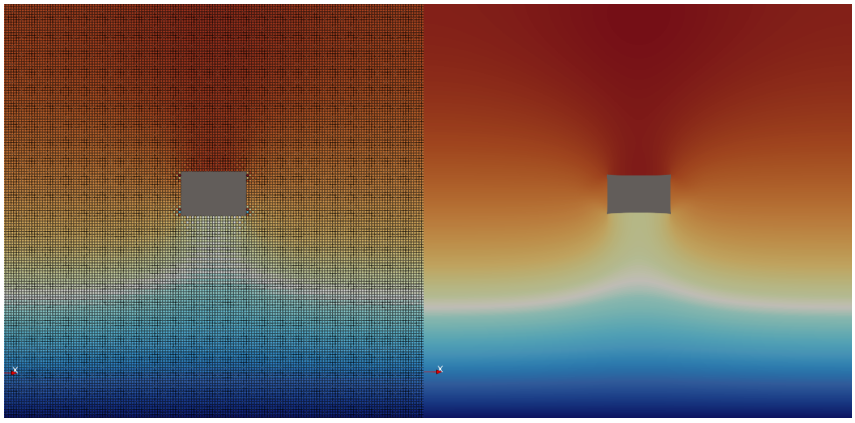


Figure 2: Vertical displacement u_z field: (a) SoliDualSPH, (b) TOCHNOG. J_2 plasticity.

The maximum equivalent plastic strain shows excellent agreement (0.091 vs. 0.10, -9%). The maximum subsidence is overpredicted by approximately 23%, which is attributed to the dynamic nature of the explicit SPH solver: inertial effects cause the soil mass to overshoot the quasi-static equilibrium. The visual fields (Figs. 1 and 2) show qualitative agreement in the plastic zone localisation and subsidence pattern.

3.2.1 Effect of stress diffusion

The stress diffusion coefficient ζ was varied over the range $[0, 1.0]$ to assess its influence on the J_2 results (Table 3).

Table 3: Sensitivity to stress diffusion coefficient ζ (J_2 case).

ζ	Max $\bar{\varepsilon}^p$	Max u_z [m]	Kinetic energy [J]
0 (off)	0.090	1.6	1.4
0.01	0.090	1.6	1.3
0.1	0.091	1.6	1.3
1.0	0.110	1.7	1.3

For the J_2 case, the results are largely insensitive to ζ: the maximum plastic strain varies by only 22% over a 100× change in ζ, and the subsidence is stable at 1.6 m. The primary effect of the diffusion is a modest reduction in kinetic energy ($1.4 \rightarrow 1.3$), indicating reduced dynamic oscillations. At $\zeta = 1.0$, the diffusion begins to artificially widen the plastic zone, slightly increasing $\bar{\varepsilon}^p$. A value of $\zeta = 0.1$ is adopted as a robust default.

3.3 Drucker–Prager plasticity: pressure-dependent validation

The Drucker–Prager validation demonstrates pressure-dependent failure. With $c = 60\,\text{kPa}$ and $\phi = 20°$, the yield threshold at the excavation roof ($I_1 \approx -424\,\text{kPa}$) is approximately 103 kPa — significantly lower than the J_2 threshold of 400 kPa. This makes the material more susceptible to dynamic oscillations near the free surface created by the excavation.

Table 4: Validation results: Drucker–Prager plasticity ($\zeta = 0.1$, $\beta_1 = 0.5$, $T_g = 30\,\text{s}$).

	SoliDualSPH	TOCHNOG	Error
Max subsidence u_z [m]	2.0	1.3	+54%
Max $\bar{\varepsilon}^p$	0.26	0.15	+73%

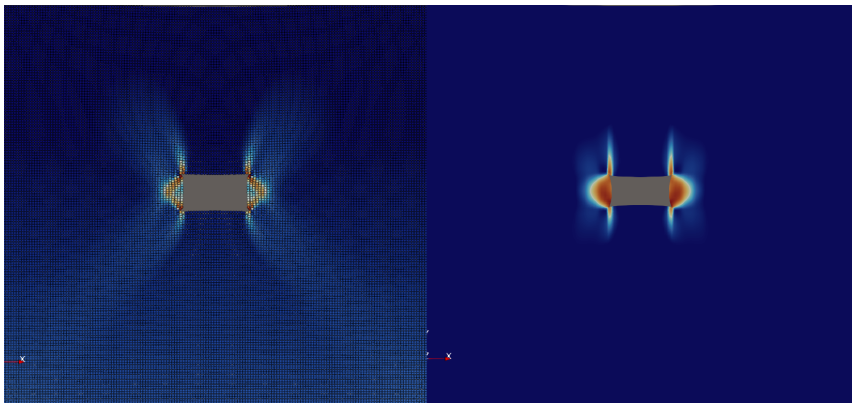


Figure 3: Equivalent plastic strain $\bar{\varepsilon}^p$ field: (a) SoliDualSPH, (b) TOCHNOG. Drucker–Prager plasticity, $c = 60\,\text{kPa}$, $\phi = 20°$, $\psi = 0°$.

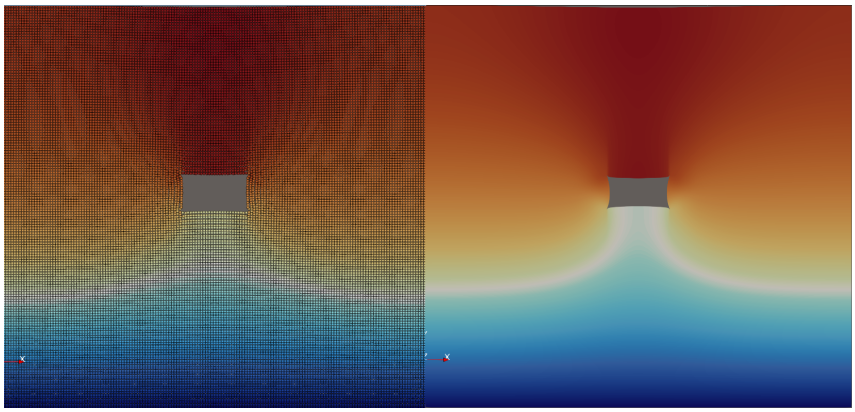


Figure 4: Vertical displacement u_z field: (a) SoliDualSPH, (b) TOCHNOG. Drucker–Prager plasticity.

The visual fields of equivalent plastic strain and vertical displacement (Figs. 3 and 4) show qualitative agreement with TOCHNOG: the plastic zone localises near the excavation roof and extends upward, and the subsidence crater forms above the chamber. However, the quantitative agreement is worse than for the J_2 case.

The larger discrepancy is attributed to the lower yield threshold of the Drucker–Prager model at low confining pressure. At the excavation roof, the yield threshold is approximately $k_c - \alpha_\phi I_1 \approx 55 - 0.112 \times (-424) \approx 103\,\text{kPa}$, compared to 400 kPa for the J_2 model. Transient dynamic oscillations of approximately 20 kPa — which are harmless for the high J_2 threshold — easily exceed the lower Drucker–Prager threshold, causing excessive plastic deformation.

3.3.1 Effect of gravity ramp duration

The gravity ramp duration was found to be the primary parameter controlling the dynamic overshoot for the Drucker–Prager case. Table 5 shows the effect of increasing T_g from 10 s to 40 s.

Table 5: Effect of gravity ramp duration on Drucker–Prager results ($\zeta = 0.1$, $\beta_1 = 0.5$, $T_{\text{excav}} = 5\,\text{s}$).

Ramp duration T_g [s]	Max $\bar{\varepsilon}^p$	Max u_z [m]
10	0.55	2.6
20	0.48	2.3
30	0.26	2.0
40	0.25	2.0
TOCHNOG	**0.15**	**1.3**

Longer ramps reduce the discrepancy significantly: $\bar{\varepsilon}^p$ decreases from 0.55 at $T_g = 10\,\text{s}$ to 0.26 at $T_g = 30\,\text{s}$, a reduction of over 50%. However, the improvement saturates beyond $T_g = 30\,\text{s}$ ($\bar{\varepsilon}^p = 0.25$ at $T_g = 40\,\text{s}$), indicating that the remaining discrepancy (+73% in $\bar{\varepsilon}^p$, +54% in u_z) is the irreducible dynamic overshoot for this problem and material configuration. Further reduction would require either implicit time integration or a configuration update procedure to refresh the reference neighbour lists under large deformation [3].

4 Discussion

4.1 Dynamic vs. quasi-static behaviour

The explicit SPH solver used in this work computes the dynamic response of the soil mass, whereas TOCHNOG solves the quasi-static equilibrium. The primary manifestation of this difference is the overprediction of subsidence: the SPH model consistently yields u_z values 20–50% higher than the quasi-static FEM reference. This overshoot is an inherent feature of explicit methods applied to slowly loaded systems: the kinetic energy accumulated during loading is not fully dissipated, and the inertia of the soil mass carries it past the static equilibrium position.

Several strategies can mitigate this effect: (i) longer gravity ramps, (ii) increased artificial viscosity, (iii) lower CFL numbers, and (iv) the stress diffusion term introduced in this work. Table 5 shows that longer gravity ramps reduce the discrepancy significantly, but the improvement saturates beyond $T_g = 30\,\mathrm{s}$, indicating an irreducible dynamic overshoot.

4.2 Role of stress diffusion

The stress diffusion term serves a dual purpose. For J_2 plasticity, where the yield threshold is high, it provides a modest damping of kinetic energy with minimal effect on the plastic strain. For Drucker–Prager plasticity, where the yield threshold at low confining pressure is significantly lower, the diffusion becomes critical: without it, dynamic stress oscillations near the excavation boundary trigger excessive spurious plasticity, leading to unphysical detachment of the soil mass above the excavation roof.

4.3 Limitations

The current implementation has several limitations:

- **Explicit time integration:** the dynamic nature of the solver causes a systematic overprediction of displacement compared to quasi-static FEM.
- **Fixed reference neighbours:** the TLSPH formulation uses neighbour lists computed in the reference configuration. For extreme deformation involving roof collapse, the fixed neighbours become ill-conditioned ($J = \det(\mathbf{F}) < 0$), leading to numerical instabilities. The configuration update procedure of Islam & Peng [3], which periodically refreshes the reference configuration and neighbour lists, is required for such cases; this extension is left for future work.
- **No particle removal:** excavated particles remain in the computational domain with reduced (10%) stiffness, rather than being physically removed.
- **2D only:** the current validation is limited to plane-strain 2D simulations.

5 Conclusion

This paper presents an activity-based excavation model implemented within the total Lagrangian SPH framework of SoliDualSPHysics. The model introduces three key features: (1) a smooth cosine-based activity transition that gradually reduces the stiffness, mass, and gravitational loading of excavated particles; (2) a Drucker–Prager plasticity model

with closed-form return mapping for pressure-dependent geomaterial behaviour; and (3) a stress diffusion stabilisation term that drives the explicit solution toward the quasi-static regime.

Validation against the FEM code TOCHNOG shows excellent agreement in the maximum equivalent plastic strain (-9% for J_2) and reasonable agreement in subsidence ($+23\%$, attributed to dynamic effects). For the Drucker–Prager case, the qualitative fields agree but the quantitative discrepancy is larger ($+73\%$ in $\bar{\varepsilon}^p$), attributed to the lower yield threshold at low confinement and the inherent dynamic overshoot of explicit time integration. The stress diffusion coefficient ζ has a modest effect on the J_2 results but is critical for the Drucker–Prager case, where it prevents spurious plasticity driven by dynamic stress oscillations.

Future work will extend the model to three dimensions, implement the configuration update procedure for extreme-deformation collapse, and investigate implicit time integration to eliminate the dynamic overshoot.

References

[1] P. A. Cundall and O. D. L. Strack. A discrete numerical model for granular assemblies. *Géotechnique*, 29(1):47–65, 1979.

[2] J. J. Monaghan. Smoothed particle hydrodynamics. *Annual Review of Astronomy and Astrophysics*, 30:543–574, 1992.

[3] Md R. I. Islam and C. Peng. A stabilized total-Lagrangian SPH method for large deformation and failure in geomaterials. *International Journal for Numerical and Analytical Methods in Geomechanics*, 2019. arXiv:1907.06990.

[4] J. Bonet and S. Kulasegaram. Alternative total Lagrangian formulations for corrected smooth particle hydrodynamics (CSPH) methods in large strain dynamic problems. *Revue Européenne des Éléments Finis*, 11(7–8):893–912, 2002.

[5] Ha H. Bui, Ryoichi Fukagawa, Kazunari Sako, and Shintaro Ohno. Lagrangian meshfree particles method (SPH) for large deformation and failure flows of geomaterial using elastic–plastic soil constitutive model. *International Journal for Numerical and Analytical Methods in Geomechanics*, 32(12):1537–1570, 2008.

[6] Ha H. Bui and Giang D. Nguyen. Smoothed particle hydrodynamics (SPH) and its applications in geomechanics: From solid fracture to granular behaviour and multiphase flows in porous media. *Computers and Geotechnics*, 138:104315, 2021.

[7] Mohammad Naqib Rahimi and George Moutsanidis. SoliDualSPHysics: An extension of DualSPHysics for solid mechanics with hyperelasticity, plasticity, and fracture. *Computer Physics Communications*, 327:110257, 2026.

[8] José M. Domínguez, Georgios Fourtakas, Corrado Altomare, Ricardo B. Canelas, Angelo Tafuni, Orlando García-Feal, Iván Martínez-Estévez, Athanasios Mokos, Renato Vacondio, Alejandro J. C. Crespo, et al. DualSPHysics: from fluid dynamics to multiphysics problems. *Computational Particle Mechanics*, 9(5):867–895, 2022.

[9] Dennis Roddeman. *TOCHNOG User's manual*. https://tochnog.sourceforge.net, 2001.

[10] E. H. Lee. Elastic-plastic deformation at finite strains. *Journal of Applied Mechanics*, 36:1–6, 1969.

[11] M. Dowell and P. Jarratt. A modified regula falsi method for computing the root of an equation. *BIT Numerical Mathematics*, 11(2):168–174, 1971.